

Simulation of the influence of surface tension on granule morphology during spray drying using a simple capillary force model

Thomas Breinlinger^a, Adham Hashibon^a, Torsten Kraft^a,

^aFraunhofer Institute for Mechanics of Materials IWM, 79108 Freiburg, Germany

Abstract

Spray drying is an important process in powder technology as it transforms fine primary powder into processable granules. While various investigations of granule formation exist, the role of surface tension on the evolution of the granule morphology has not been investigated in much detail. This work closes this gap by using numerical simulations on granule level. In our simulation of suspensions of solid particles we use the Discrete Element Method (DEM) in combination with a CFD solver. Due to the free liquid surface, a multiphase solver is needed including a force model for the particle-surface contact. As a result, our work gives insight into the granule formation and reveals a clear non-linear dependency relating high surface tension to dense granules.

Keywords: Spray drying, granulation, morphology, surface tension, capillary force

1. Introduction

Spray drying is an important process in powder technology, e.g. in the ceramic industry. In the latter, the raw material often is available in the form of a very fine primary powder, which is highly adhesive due to the small particle size. Therefore it has to be transformed to coarser granules which is often done using the spray drying process [1]. In order to achieve good handling and compacting properties of the granulate, the individual granules are often required to be spherical and dense, allowing for good quality of the final product. Hollow granules, on the other hand, can create voids due to bad compressibility [2], which could create defects inside the sintered product and reduce its strength [3].

Numerous experimental investigations showed that the stability of the suspension has a major influence on the granule morphology evolving during spray drying, i.e. well dispersed suspensions often lead to hollow granules [4–7]. Hence, the interparticle forces and the solvent-particle interaction play an important role in the evolution of the granule morphology. In addition, the capillary force exerted on the primary particles by the receding liquid surface creates a compressive drying stress inside the particle network [8]. Therefore, the capillary force may also have a

Email address: thomas.breinlinger@iwm.fraunhofer.de (Thomas Breinlinger)

significant effect on the granule development. However, this force has not been studied experimentally in the context of spray drying of ceramics, which might be caused by the difficulty of varying the surface tension without changing other important suspension parameters.

The experimental investigations have been supplemented by a number of simulation studies on granule formation during spray drying. The different methods proposed in the literature are discussed in the following.

Basic approaches use one dimensional models of heat and mass transfer [9, 10] to describe the drying of rotationally symmetric drops depending on the suspension parameters and process conditions. By taking into account transport through porous media in a growing outer zone of the drop it is possible to even simulate shell formation to some extent [11]. These models can be used to calculate the drying kinetics, which may then be used in process scale simulations for the tracking of drying granules through the drying chamber. However, more detailed information about the evolution of the granule morphology on particle level cannot be gained by such mean-field models.

A more enhanced class of models uses a stochastic description of the suspended particles based on a population balance [12]. This continuum mechanical approach allows e.g. for distinguishing between wet and dry shell and enables the simulation of shell growth [13] and even provides some insight in the granule morphology [14].

In contrast to the above methods, the discrete element method (DEM) may be used to study the morphology of particle based systems in much more detail [15], as it describes the solid content as many individual particles. E.g., Greil et al. [15] used it to simulate the electrophoretic deposit of solids on a substrate and Breinlinger et al. [16] simulated the deposit formation at the drying of suspensions on a substrate using a similar method. Recently, the DEM has been applied to study the granule formation during spray drying [17, 18] by coupling it to computational fluid dynamics (CFD). These simulations showed a trend to hollow granules for higher temperatures [17] and higher binder content [18].

For the simulation of coupled CFD-DEM problems, the interaction between the fluid and particle phase is described by coupling forces, e.g. drag, buoyancy etc. If the fluid phase itself consists of two continuous phases, i.e. gas and liquid as in the case of spray drying, additional coupling forces are needed at the liquid surface. This capillary force and the resulting surface curvature has been studied previously and models for thin layers of suspensions on a substrate can be found in literature [19, 20]. A full description of the contact between a particle and the liquid surface by this model requires knowledge about either the external conditions (i.e. present forces) or the geometry (i.e. neck curvature, height, length etc.). However, in our case the neck geometry and the capillary force is unknown.

None of the aforementioned works – neither experimental nor numerical – investigated the role of surface tension on the formation of spray dried ceramic granules. Therefore, in this work we aim to investigate this in detail. For this purpose we implemented a coupled CFD-DEM solver, which is based on OpenFOAM® [21], an open source CFD software package. We simplify the coupling conditions by neglecting local curvatures in order to be able to simply derive the required coupling force from the pressure gradient and line tension acting on the particle.

2. Methods

2.1. The Discrete Element Method

In this work we use the Discrete Element Method (DEM) [22] to describe the granular media. This method describes the motion of an individual solid particle based on Newton's equations of motion

$$\dot{\mathbf{p}} = \mathbf{F}, \quad (1)$$

where \mathbf{p} is the linear momentum and \mathbf{F} is the sum of external forces. The DEM model treats each solid particle as an individual particle and calculates their trajectories by integrating equation 1 in time

$$m_i \dot{\mathbf{v}}_i = \sum_{n,j} \mathbf{F}_{ij}^n + \mathbf{F}_i^{\text{coupling}}, \quad (2)$$

where m_i and \mathbf{v}_i denote the mass and velocity of particle i , respectively, \mathbf{F}_{ij}^n represents the n different interaction forces between particles i and j and $\mathbf{F}_i^{\text{coupling}}$ is the coupling force for momentum exchange with the fluid phase. Brief general reviews of DEM contact forces are available e.g. from [23] and [24]. In the following, we describe the contact force model used in our approach. The rotation of particles was not taken into account as we suppose that it would be only of minor influence on the particle reorganisation and [25] showed that a rotational degree of freedom can actually hinder the development of a steady state system due to numerical reasons. The friction coefficient was used to mimic non-spherical particle shape.

2.2. Contact force model

Contact forces between two individual DEM particles with radius r are applied whenever these particles have a positive overlap

$$h_{ij} = x_{ij} - (r_i + r_j) \quad (3)$$

where x_{ij} is the magnitude of the distance $\mathbf{x}_{ij} = \mathbf{x}_i - \mathbf{x}_j$ between the centre points \mathbf{x}_i and \mathbf{x}_j of the particles. The contact model used in this work consists of elastic repulsion, repulsion dissipation, cohesion and friction. The elastic repulsion is described following [26] as

$$\mathbf{F}_{ij}^e = \left(2/3 \bar{E} \sqrt{\bar{r}_{ij}} h_{ij}^{3/2} \right) \hat{\mathbf{x}}_{ij}, \quad (4)$$

in normal direction $\hat{\mathbf{x}}_{ij} = \mathbf{x}_{ij} / |\mathbf{x}_{ij}|$. Here $\bar{r}_{ij} = r_i r_j / (r_i + r_j)$ represents the effective particle radius and $\bar{E} = E / (1 - \nu^2)$ is the effective Young's modulus with the Poisson number ν . The viscous part of the collision, which represents dissipation by plastic deformation and noise emission, is modelled as a velocity dependant damping force [27]

$$\mathbf{F}_{ij}^v = - \left(\gamma \sqrt{\bar{r}_{ij}} h_{ij} \mathbf{v}_{ij} \cdot \hat{\mathbf{x}}_{ij} \right) \hat{\mathbf{x}}_{ij}. \quad (5)$$

The damping parameter γ is determined empirically. Cohesion between the particles is modelled based on the overlap area A of the contact

$$\mathbf{F}_{ij}^c = - (\omega_{AA}) \hat{\mathbf{x}}_{ij}, \quad (6)$$

where ω_A is the cohesive force per unit area or work per unit volume. Friction between the DEM particles is modelled following [22] as a tangential force

$$\mathbf{F}_{ij}^f = -\min \left[k \sqrt{\frac{h_{ij}}{\bar{r}_{ij}}} |\xi_{ij}|, \mu |\mathbf{F}_{ij}^e + \mathbf{F}_{ij}^v| \right] \frac{\xi_{ij}}{|\xi_{ij}|} \quad (7)$$

based on the relative displacement ξ_{ij} of the initial contact points its magnitude is governed by the tangential spring constant k and the friction parameter μ .

2.3. The volume of fluid method

The volume of fluid method (VoF) for multiphase flow [28] can be used to describe the motion of two immiscible fluids. It can be combined with the discrete element method by using locally averaged coupling [29] which will be described in section 2.4. In this context, the motion of two incompressible fluid phases, e.g. water and air, carrying solid particles is governed by the averaged Navier-Stokes equations

$$\nabla \cdot \mathbf{v} = 0 \quad (8)$$

$$\rho \frac{D\mathbf{v}}{Dt} = -\nabla p + \eta \nabla^2 \mathbf{v} + \sigma \kappa \frac{\nabla \alpha}{|\nabla \alpha|} + \rho \mathbf{g} + \mathbf{f}_c, \quad (9)$$

where \mathbf{v} is the velocity, p is the pressure and \mathbf{g} is the gravity. Surface tension is included by the term $\sigma \kappa \nabla \alpha / |\nabla \alpha|$, where σ is the surface tension coefficient and κ is the curvature of the liquid surface. The term \mathbf{f}_c represents volumetric coupling forces from the solid particles and will be discussed later. The average density ρ and dynamic viscosity η in each cell are computed as

$$\rho = \rho_l \alpha + \rho_g (1 - \alpha), \quad \eta = \eta_l \alpha + \eta_g (1 - \alpha), \quad (10)$$

based on the phase function α , which determines the ratio of water in each cell. The indices l and g represent the liquid and gas phase, respectively. The phase function ranges from 0 to 1 and is balanced by its own transport equation

$$\frac{\partial \alpha}{\partial t} + \nabla \cdot \mathbf{v} \alpha = \dot{\alpha}_{ev}, \quad (11)$$

where the $\dot{\alpha}_{ev}$ is a source term which extends the established VoF scheme to incorporate evaporation during the drying process (see section 4). This source term has the form

$$\dot{\alpha}_{ev} = -\frac{1}{2} D \kappa \frac{(c_f - c_\infty)}{\rho_l} |\nabla \alpha|, \quad (12)$$

where D is the diffusion coefficient and c_f and c_∞ are the vapour concentrations in the evaporation film and at ambient conditions, respectively. For the sake of boundedness of the phase function and stability of the solution, the application of $\dot{\alpha}_{ev}$ was limited to regions where $0 \leq \alpha \leq 1$. The evaporation is described as isothermal and diffusion controlled. The former seems to be a justified assumption, as it has been shown that the temperature of a spray dried drop is almost constant over most of the drying time [30]. The latter assumption is true in the beginning but will be violated once the fluid surface penetrates the granule surface and transport in a porous medium occurs. This is an intrinsic restriction of the locally averaged coupling method because

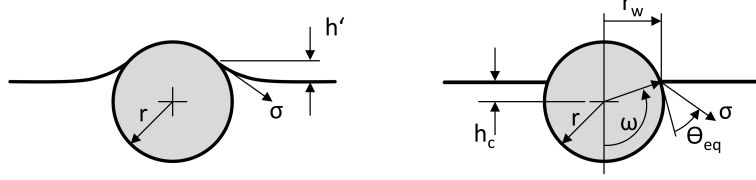


Figure 1: Schematic illustration of a particle-surface contact. Left: Real contact with capillary neck. Right: Contact with negligible local curvature as assumed by the model.

the localized transport phenomena are below cell level and, hence, cannot be resolved. However, it still appears to be a reasonable approach for spray drying because some of the dominating effects determining the granule morphology (i.e. shell formation and shell stability) happen in the early stages of drying where the model is valid.

The solver is implemented in OpenFOAM® [21], version 2.2.1, as a combination of the standard solvers *interFoam* and *icoUncoupledKinematicParcelFoam*, which originally treat two fluid cases (*interFoam*) and uncoupled or single fluid coupled particle simulations *icoUncoupledKinematicParcelFoam*, respectively. Due to the modular architecture of OpenFOAM® with the basic functions for coupling already implemented it is straight forward to implement e.g. new forces using existing models as a blueprint. The relevant forces and their application are described in the following section.

2.4. The coupling force model

The coupling between CFD and DEM was established based on cell level averaging [29], i.e. the volumetric coupling force \mathbf{f}_c in the momentum equation (9) was calculated for each cell as the sum of the total coupling force $\mathbf{F}^{coupling}$ of all DEM particles inside the cell

$$\mathbf{f}_c = \mathbf{F}^{coupling} / V_{cell}. \quad (13)$$

Here V_{cell} is the volume of the computational cell. The individual coupling forces are described in the following.

In cases where a relative velocity between the fluid and the particles exists, the drag force must be included in the coupling. For this dissipative component of momentum coupling Stoke's law for the fluid particle drag force

$$\mathbf{F}_i^s = 6\pi\eta r_i \mathbf{v}_{rel,i} \quad (14)$$

with $\mathbf{v}_{rel,i}$ representing the relative velocity between particle i and the surrounding fluid was implemented here and used in the validation case in section 3.2. However, it was neglected in the spray drying simulations in section 4 because of numerical reasons. In those cases there is no significant physical current inside the fluid because it only evaporates at the surface. In contrast, due to the VoF model, there are intrinsic artificial currents [31–33] that can induce a significant error on the particle formation. Therefore, the drag force was turned off during the simulations presented in section 4.

For particles at the drop surface figure 1 shows on the left a schematic illustration of the particle-surface-contact. On such contact, two different forces arise: the pressure force and the capillary force. For single particle contacts, these forces can be derived in the style of the investigation of capillary bridges by [20] as follows.

The curvature κ of the interface leads to a pressure jump Δp across the surface which is described by the Young-Laplace equation

$$\Delta p = 2\sigma\kappa, \quad (15)$$

where σ is the surface tension and κ again is the curvature which, for a sphere of radius R , is defined as $1/R$. For a particle protruding from the surface, this pressure difference relates to a net force normal to the surface

$$\mathbf{F}^{\Delta p} = A_w \Delta p \hat{\mathbf{n}}, \quad (16)$$

where A_w is the cross sectional area at the intersection plane, which is a circle with wetting radius r_w and $\hat{\mathbf{n}}$ is the surface normal. Figure 2 (a) shows this pressure force for different particle sizes plotted over the radius of the spherical water drop on which the contact happens. The contact angle has been set to $\Theta = 90^\circ$, which yields $r_w = r$. The increase of pressure towards smaller drop radii results from equation 15, where the curvature κ is inversely proportional to the drop radius R .

The capillary force results from the line contact of the liquid surface and the particle, where the surface tension of the liquid applies line tension to the particle. If the local curvature and the size of the neck h' (figure 1, left) are small (i.e. the surface tension is small or the contact is close to equilibrium) the neck can be neglected and the contact can be approximated as illustrated in the right hand side of fig. 1. Although the local curvature is neglected, the surface tension σ still applies in its original direction. The angle between the vertical axis and the direction of σ is $\omega - 90^\circ + \Theta$, as Θ is measured from a plane perpendicular to ω .

The net force acting on the particle caused by σ can be calculated as the integral of the surface tension along the line of contact [34]

$$\mathbf{F}^{cap} = \int \sigma dl \hat{\mathbf{n}}, \quad (17)$$

where l runs along the contact line. For a spherical particle, the radial component is cancelled out along the circumference and the vertical component of the force $F_v^{cap} = \sigma_v U$ is equal to the vertical component of the surface tension σ_v and the length of the contact line U . The vertical component of the surface tension can be calculated as $\sigma_v = \sigma \sin(\omega + \Theta)$ and the length of the contact line is $U = 2\pi r_w$, where the wetting radius r_w can be determined by $r_w = r \sin(\omega)$. Hence, the capillary force acting on the particle is approximated as

$$\mathbf{F}^{cap} = 2\pi r \sigma \sin(\omega) \sin(\omega + \Theta) \hat{\mathbf{n}}. \quad (18)$$

Figure 2 (b) shows this capillary force for a particle of $r = 10 \mu m$ on a water surface for different equilibrium contact angles Θ .

The wetting angle ω is given by $\omega = \arccos(-h_c/r)$. Here h_c is the distance of the particle centre from the liquid surface. If the liquid surface is given analytically, the calculation of h_c is trivial. If it is provided by a scalar field, e.g. the phase function α used in the volume of fluid method [28], it can be evaluated from the gradient of this scalar as $h_c = (\alpha_b - \alpha_p) / |\nabla \alpha_p|$, where α_p is the scalar value at the particle and α_b represents the phase boundary. In the context of volume of fluid, where $0 \leq \alpha \leq 1$, this boundary is at $\alpha_b = 0.5$.

It is important to note that by neglecting the local necks at the particle-surface-contacts in the derivation of equation 18 we also neglect their contribution to the drop pressure, which would normally decrease considerably due to the concave curvature. If this had not been done, the

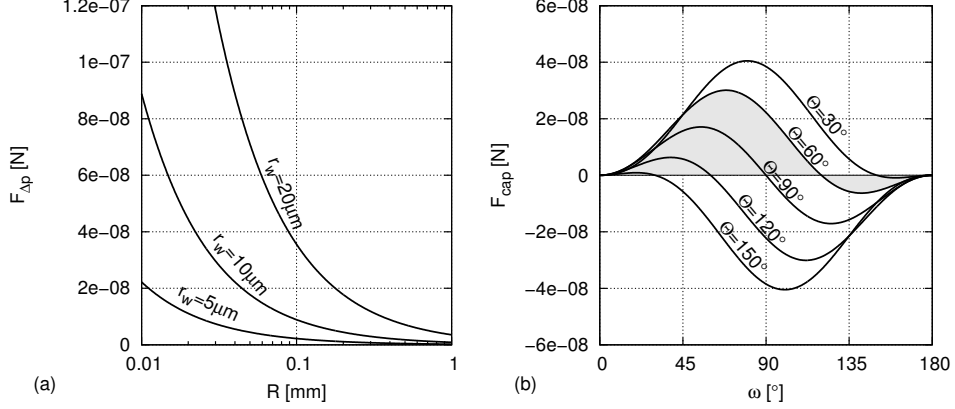


Figure 2: Particle-fluid forces at the liquid surface. (a): Pressure force as a function of the drop radius R for different particle sizes r_w . (b): Capillary force as a function of the relative position ω for different wetting angles Θ (see figure 1 for definition of ω).

particles would be ejected during shrinkage due to the high pressure at small drop sizes seen in figure 2 (a). Consequently, in this context it is necessary to remove $\mathbf{F}^{\Delta p}$ (equation 16) from the system because the underlying pressure does not include these localized effects. I.e. either we take into account both pressure force and local curvature, which is not possible in the locally averaged approach, or we neglect both as done in this work.

A second consequence resulting from neglecting the local necks is that tangential forces due to multiple particle-surface-contacts are also not considered. Although there are recent works on this topic based on flat surfaces [35] (i.e. drying on a substrate), these forces are quite hard to estimate on an arbitrary curved fluid surface, especially once the surface penetrates the particle network. However, although these tangential forces may play a role in the particle formation in the initial phase, it is assumed that their influence on the overall granule morphology is limited and, hence, that they may be neglected.

A possibility to drop the aforementioned assumptions and restrictions resulting from neglecting the local necks at the particle-surface-contacts would be to use a highly resolved simulation method, where the grid is much finer than the particles and, consequently, the fluid interaction around and between the particles would be fully resolved. This would allow for a more detailed simulation of both surface tension and capillary forces as well as the evaporation by transport through porous media. However, the reason for not using this approach in this work is that the gain in accuracy is bought by massive computational requirements and cost resulting in a limited system size that does not allow for the simulation of entire granules.

3. Validation

3.1. Energy balance

In the absence of other influences, the change of energy which a particle experiences on crossing the liquid surface can be calculated as the integral of the capillary force along the particle

Parameter	Unit	Section 3.1	Section 3.2
Particle radius	$[\mu\text{m}]$	10	10
Fluid viscosity	$[\text{mPa s}]$	0	5, 10, 25
Particle density	$[\text{g/cm}^3]$	2	2
Initial velocity	$[\text{m/s}]$	1, 2, 3, 4, 5	0
Initial height	$[\mu\text{m}]$	20	0
Wetting angle	$[\text{°}]$	0, 30 . . . 180	0, 30 . . . 180
Surface tension	$[\text{mN/m}]$	70.7	70.7

Table 1: Simulation parameters for the validation test cases.

trajectory

$$E_{cap} = \int F_{cap}(h) dh. \quad (19)$$

For a full passage, integration within the limits $[-r, r]$ yields

$$E_{pass} = \frac{3}{4}\pi^2\sigma r^2 \cos(\Theta). \quad (20)$$

Figure 3 (a) shows E_{pass} as a function of the equilibrium wetting angle Θ .

As a first test, this energy is evaluated for simulations where a particle was placed above a fixed liquid surface, which means that the VoF part of the solver was inactive and momentum transfer only occurred towards the particles. These were given an initial velocity towards the fixed surface. The surface was flat, which corresponds to an infinite curvature and zero pressure jump from equation 15. Drag forces were neglected in these test cases to isolate the capillary force. Table 1 shows the set-up parameters.

The theoretical final velocity of a particle after the surface contact can be calculated from the initial kinetic energy and the capillary energy (equation 20) as

$$v = \sqrt{\frac{1}{2}mv_0^2 + \frac{3}{4}\pi^2\sigma r^2 \cos(\Theta)}. \quad (21)$$

The final velocities have been extracted from 35 simulations with initial velocities of $v_0 = 1 \dots 5 \text{ m/s}$ and equilibrium wetting angles of $\Theta = 0 \dots 180^\circ$. The results are plotted as squares in figure 3 (b) along with the exact values (solid lines). Comparing these results, the simulation shows good agreement with the exact values over the entire range of velocities and wetting angles. For cases where the initial kinetic energy was not high enough for the particle to pass the liquid surface, the particle was repelled. Here, the error was within the computational accuracy.

3.2. Pinning and steady state

In the second test case, we test our model against the steady state of particle-fluid surface dynamics. To mimic a pinned particle contact, we place the particle with its centre on the fixed liquid surface and release it at the beginning of the simulation. For varying wetting angles Θ and fluid viscosities η , which are given in table 1 along with the other parameters, the particle position was monitored. As an example, figure 4 shows a series of snapshots of the oscillating behaviour between the initial position at $t = 0 \text{ ms}$ and the final position at $t = 100 \text{ ms}$.

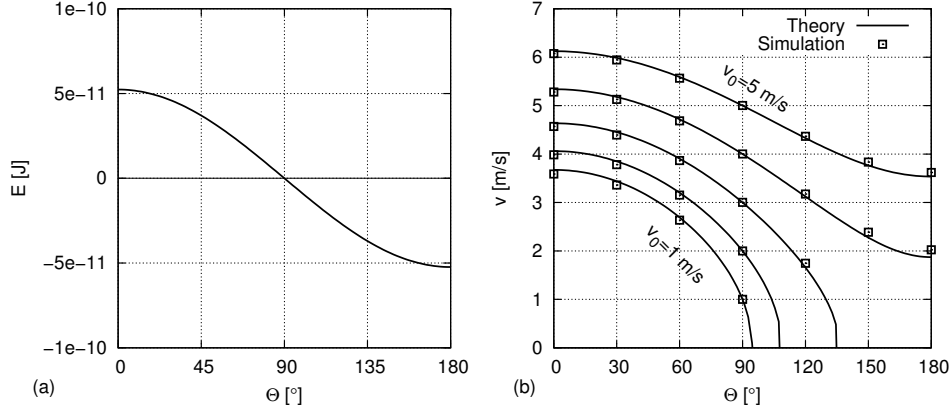


Figure 3: (a): Energy balance of a particle crossing a steady liquid surface. (b): Final velocities of particles after crossing a surface with varying initial velocities and wetting angles.

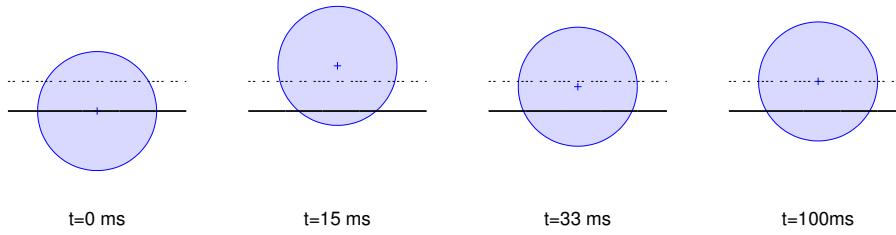


Figure 4: A series of snapshots for $\Theta = 120^\circ$ and $\eta = 5$. Blue spheres: particles, solid lines: liquid surface, dashed line: equilibrium position.

For all the test cases, figure 5 shows the evolution of the particle positions during the simulations (solid lines) along with the equilibrium positions (dashed lines). At wetting angle $\Theta = 90^\circ$, the system remains at rest as it already is at its equilibrium position. For moderate contact angles of $\Theta = 60^\circ$ and 120° , the particles reach a steady state position according to the equilibrium position. While the evolution happens smooth and steady at high viscosity, there are some oscillations at lower viscosities. In the more hydrophobic and hydrophilic cases ($\Theta = 180^\circ - 150^\circ$ and $\Theta = 0^\circ - 30^\circ$, respectively), the energy initially stored in the contact is larger so that during particle movement more energy has to be dissipated in order to reach pinning at equilibrium. This is the case for $\eta = 25$ mPas and, consequently, the particles reach steady state pinning. For $\eta = 5$ and 10 mPas, the dissipation is not sufficient and particles get ejected from the surface. In the case of $\eta = 5$ (figure 5 b) the ejected particles have not much momentum left due to the higher viscosity and, consequently, get decelerated quickly by the drag force.

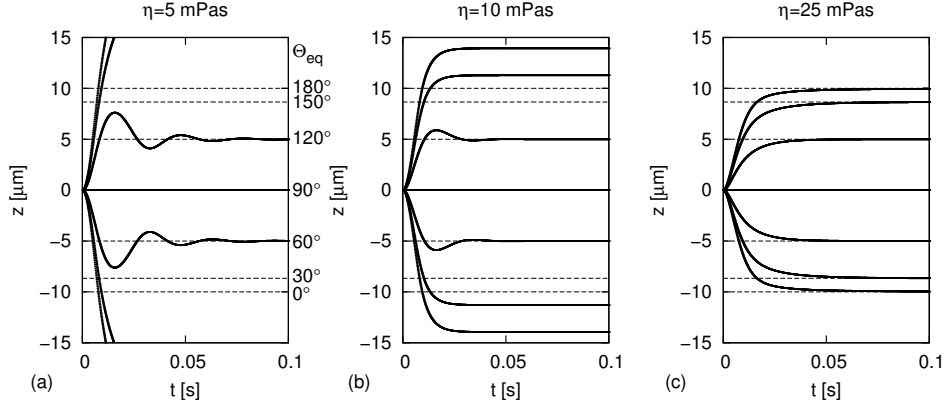


Figure 5: Effect of wetting angle and viscosity on the dynamics of a particle contact with a steady liquid surface. Solid lines: simulations, dashed lines: equilibrium position.

4. Application to spray drying

Finally, we apply our model to the simulation of drying drops of ceramic suspensions using a solver that couples the DEM scheme with the volume of fluid (VoF) method.

The set-up of the 3D simulations consists of a cubic box of 1 mm edge length discretized with 30 cells per direction. At the centre of this box, a drop of 500 μm diameter was placed and filled with 30 vol% of solid particles of 20 μm diameter. The particles were placed randomly but without initial overlap. A preliminary study with varying particle positions showed that their initial arrangement has only a minor influence on the granule morphology. While 30 vol% is a popular value [e.g. 4, 36], the usual particle size of 1 μm was not possible to model as this would result in a number of particles which is much too high for the numerical simulation. In cases where the number of particles is too large for a DEM simulation, it is a common technique to artificially coarsen the particles (*coarse graining*) in order to obtain a computable system [25]. Therefore, the DEM particles were coarse grained to 20 μm , which reduces the number of particles from approximately 38m to only 4900 in the simulation. As these coarse grained particles represent a number of real particles, their density was reduced from 3.94 g/cm^3 (Al_2O_3) to 2 g/cm^3 . The friction coefficient was set to the quite high value of 2 in order to mimic the real non-spherical shape of the primary particles. The cohesion parameters reflect the bulk cohesion of the primary particles and are generic model parameters. A reasonable parameter space has been identified in preliminary test runs. A more in depth discussion of the coarse graining and the interpretation of the cohesion model can be found in [37]. The carrier fluid was chosen to be water as often used in the ceramic industry [e.g. 7, 8]. However, the fluid viscosity η was increased by two orders of magnitude in order to reduce the numerical artefacts mentioned in section 2.4 which are intrinsic to the surface tension model [31–33]. In the present case this appears legit as the system is controlled by surface tension and viscous effects play only a minor role. The damping parameter has been adopted from the corresponding example cases of OpenFOAM. As inertia effects are very small in the present cases, this parameter is only of minor influence. The simulation parameters are summarized in table 2.

Within this study, we used two different cohesion parameters: a wet cohesion ω_i and a dry

Parameter	Unit	Section 4
Drop diameter	μm	500
Solid content	<i>vol%</i>	30
Fluid density	g/cm^3	1
Fluid viscosity	$Pa s$	0.1
Diffusion coefficient	mm^2/s	20.7
Temperature	$^{\circ}C$	150
Particle density	g/cm^3	2
Wetting angle	$^{\circ}$	60
Cohesion dry	kN/m^2	150
Cohesion wet	kN/m^2	0...150
Surface tension	mN/m	0.707...70.7
Particle diameter	μm	20
Friction coefficient	–	2
Young's modulus	$[N/m^2]$	$1.7 \cdot 10^6$
Poisson ratio	[–]	0.35
Damping parameter	$[Pa s]$	0.2

Table 2: Simulation parameters for the simulation of spray drying.

cohesion ω_o in order to mimic the complex particle contacts in real suspensions and dried granules, respectively. While the dry cohesion was kept constant in the simulations shown here, the wet cohesion ω_i was varied to 0, 10, 50 and 100% of the dry cohesion ω_o , corresponding to $\omega_i/\omega_o = 0, 0.1, 0.5$ and 1. This was done in order to have a variety of granule morphologies as a base for variations of the capillary force.

The goal of this study was to identify the influence of the capillary force on the formation of spray dried granules. Hence, the capillary surface tension was varied in the next step within $\sigma = \{1/10, 1/3, 1, 3, 10\} \sigma_0$, where $\sigma_0 = 7.07 mN/m$. As a result, figure 6 shows cross sections through the three granules with $\sigma/\sigma_0 = 0.1, 1$ and 10. The slices shown here have a thickness of roughly two particles. We observe a dense granule for high capillary surface tension ($\sigma = 10\sigma_0$) whereas a granule with internal voids result from for medium ($\sigma = \sigma_0$) and low ($\sigma =$

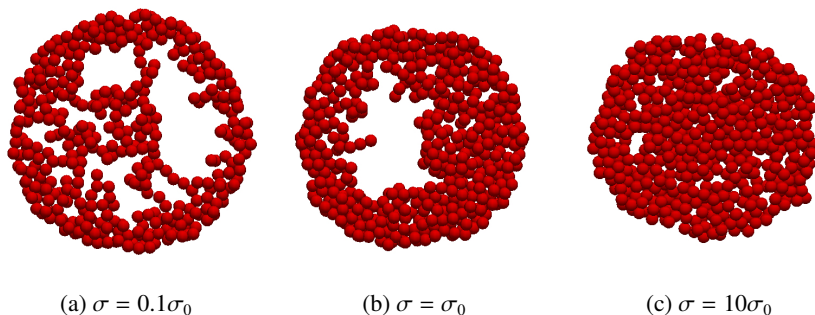


Figure 6: Cross sections through the base granules ($\omega_o = 150 kN/m^2$, $\omega_i/\omega_o = 0.5$) with a thickness of roughly two particles.

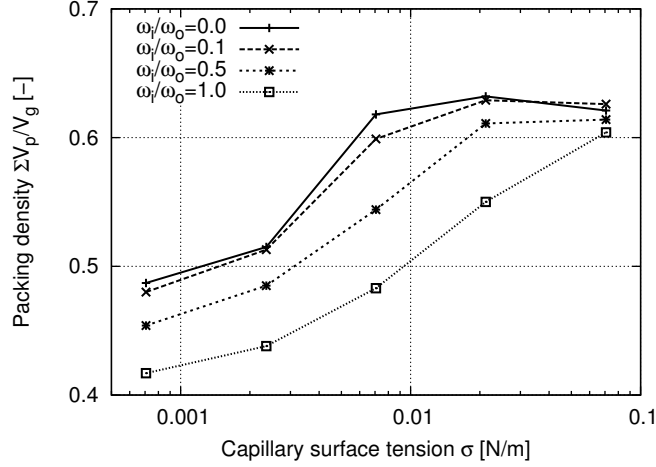


Figure 7: Mean packing density of dried granules as a function of the capillary surface tension σ .

$0.1\sigma_0$) surface tensions. For the medium surface tension the particles in the interior gather at the surrounding shell, while at $\sigma = 0.1\sigma_0$ some thin networks remain inside the granule.

The resulting granules were evaluated in terms of packing density. High packing densities correspond to dense granules whereas hollow and porous granules correspond to low packing densities. Figure 7 shows the packing density of the resulting granules as a function of the capillary surface tension for the different wet cohesions. In figure 7 we can see the base granules from figure 6 represented by a column of points at $\sigma = 0.00707 \text{ N/m}$ corresponding to the different granule morphologies.

Furthermore, we observe a strong dependency of the granule density on the capillary surface tension relating low surface tensions with low densities and high surface tensions with high densities. The correlation is not linear, however. Indeed the mode of correlation itself depends on the cohesion as we observe a relatively smooth transition for high wet cohesions opposed to a rather sharp, almost step-like transition for low wet cohesion.

On top of this non-linear correlation, we find the range of the granule densities for different cohesions to also depend on the capillary surface tension. At the base parameter $\sigma = \sigma_0$ we observe a relatively large variation of 13.5%. A low surface tension of $\sigma = 0.1\sigma_0$ results in a range of the granule densities of 7% while a high surface tension of $\sigma = 10\sigma_0$ reduces the range to 2.2%.

5. Discussion

The drying of drops of ceramic suspensions in the spray drying process yielding solid granules has been investigated thoroughly in the past. However, in the majority of the reports, both experimental [2–7] and simulation [9–14, 17, 18], the influence of surface tension has not been studied in any detail. It was part of the idea of this study to close this gap using simulations, but on the other hand, this lack of experimental data makes it hard to carry out immediate validation of the results by experimental data.

Nonetheless, our results provide reasonably plausible qualitative insight into the mechanisms of granule formation and provide a clear correlation between capillary surface tension and the resulting granule morphology: As evaporation takes place, the solid particles are pushed towards the centre of the drop by the receding liquid surface, which corresponds to a concentration of particles beneath the drop surface. As the drying goes on, the evolution of the granule is dominated by two effects: (i) the formation of a more or less stable shell whose physical strength is dominated by cohesion and (ii) the compressive stress exerted on this network of particles by the capillary surface tension. Hence, if the compression is strong enough against the cohesive network, some bonds may break yielding ductile deformation and rearrangement of the particles which leads to solid granules. In turn, if the strength of the cohesive bonds is strong against the capillary stress, the particle network may withstand the external load and the surface penetrates the shell, leading to a hollow and porous granules.

Corresponding with experimental findings [e.g. 36, 38], our simulations show the formation of internal voids inside the granules (see figure 6). These voids are generated during the drying process. Usually, the particles are randomly distributed within the drop, so that no initial voids exist. The mechanism forming the large internal voids is that once the outer shell is strong enough, the liquid surface penetrates the granule and at some point the drying process may lose its symmetry. I.e., the capillary forces transport the particles to one certain region inside the granule and therefore creates a void elsewhere. Corresponding experimental results showing hollow granules with a lump of material on the inside can be found in literature [e.g. 36].

The influence of the evaporation rate has not been studied in this work. This might be an interesting aspect to be addressed in future work.

6. Summary and Conclusions

A capillary force model was derived for particles in contact with liquid surfaces. It is based on the Young-Laplace and Young equations and requires the capillary necks to be negligible.

The validation of the particle-surface contact model implementation showed good agreement with theory in terms of energy conservation and the steady state pinning of particles at the surface.

The model was implemented into a coupled DEM-VoF solver and applied to the drying of spherical drops of ceramic suspensions as a representative model for granule formation in the spray drying process. The variation of the capillary surface tension revealed a non-linear correlation with the resulting granule density and morphology relating high surface tensions to dense granules and vice versa. This clearly suggests that surface tension is an important parameter in spray drying and that it should not be neglected in product and process design. An explanation of the results was provided that extends the established concept of particle mobility [4, 36, 38] by the influence of shell stability.

7. Acknowledgement

This research has been partially supported by the EU FP7 Project SimPhoNy (grant number 604005) and the German Research Foundation (DFG) under grant WO 1667/1-1.

References

- [1] S. Lukasiewicz, Spray-drying ceramic powders, *Journal of the American Ceramic Society* 72 (4) (1989) 617–624.

- [2] S. Lukasiewicz, J. Reed, Character and compaction response of spray-dried agglomerates, *American Ceramic Society Bulletin* 57 (1978) 798–801.
- [3] J. Reeds, Spray drying and implications for compactibility of product granules, *Ceramic Engineering and Science Proceedings* 18 (1997) 343–358.
- [4] W. J. Walker Jr., J. S. Reed, S. K. Verma, Influence of slurry parameters on the characteristics of spray-dried granules, *Journal of the American Ceramic Society* 82 (7) (1999) 1711–1719.
- [5] J. Tsubaki, H. Yamakawa, T. Mori, H. Mori, Optimization of granules and slurries for press forming, *Journal of the Ceramic Society of Japan* 110 (2002) 894–898.
- [6] F. L. G.E. Fair, Effect of interparticle potential on forming solid, spherical agglomerates during drying, *Journal of the American Ceramic Society* 87 (2004) 4–9.
- [7] G. Bertrand, P. Roy, C. Filiatre, C. Coddet, Spray-dried ceramic powders: A quantitative correlation between slurry characteristics and shapes of the granules, *Chemical Engineering Science* 60 (1) (2005) 95 – 102.
- [8] J. A. Lewis, Colloidal processing of ceramics, *Journal of the American Ceramic Society* 83 (10) (2000) 2341–2359.
- [9] A. Lee, C. Law, Gasification and shell characteristics in slurry droplet burning, *Combustion and Flame* 85 (1-2) (1991) 77–93.
- [10] M. Kadja, G. Bergeles, Modelling of slurry droplet drying, *Applied Thermal Engineering* 23 (7) (2003) 829–844.
- [11] H. Liang, K. Shinohara, H. Minoshima, K. Matsushima, Analysis of constant rate period of spray drying of slurry, *Chemical Engineering Science* 56 (6) (2001) 2205–2213.
- [12] C. S. Handscomb, M. Kraft, A. E. Bayly, A new model for the drying of droplets containing suspended solids, *Chemical Engineering Science* 64 (4) (2009) 628–637.
- [13] C. S. Handscomb, M. Kraft, A. E. Bayly, A new model for the drying of droplets containing suspended solids after shell formation, *Chemical Engineering Science* 64 (2) (2009) 228–246.
- [14] C. S. Handscomb, M. Kraft, Simulating the structural evolution of droplets following shell formation, *Chemical Engineering Science* 65 (2) (2010) 713–725.
- [15] P. Greil, J. Cordelair, A. Bezold, Discrete element simulation of ceramic powder processing, *Zeitschrift Für Metallkunde* 92 (7) (2001) 682–689.
- [16] T. Breinlinger, P. Polfer, A. Hashibon, T. Kraft, Surface tension and wetting effects with smoothed particle hydrodynamics, *Journal of Computational Physics* 243 (2013) 14–27.
- [17] D. Nishiura, A. Shimosaka, Y. Shirakawa, J. Hidaka, Simulation of drying of particulate suspensions in spray-drying granulation process, *Journal of Chemical Engineering of Japan* 43 (8) (2010) 641–649.
- [18] S. Miyazaki, D. Nishiura, A. Shimosaka, Y. Shirakawa, J. Hidaka, Revealing the formation mechanism of granules by drying simulation of slurry droplet, *Advanced Powder Technology* 22 (1) (2011) 93–101.
- [19] P. A. Kralchevsky, K. Nagayama, Capillary forces between colloidal particles, *Langmuir* 10 (1) (1994) 23–36.
- [20] P. Kralchevsky, K. Nagayama, *Particles at fluid interfaces and membranes*, Elsevier, 2001.
- [21] OpenFOAM Foundation, OpenFOAM@documentation, www.openfoam.org (2014).
- [22] P. Cundall, O. Strack, A discrete numerical model for granular assemblies, *Geotechnique* 29 (1) (1979) 47–65.
- [23] S. Luding, About contact force-laws for cohesive frictional materials in 2d and 3d, in: P. Walzel, S. Linz, C. Krülle, R. Grochowski (Eds.), *Behavior of Granular Media*, Shaker Verlag, 2006, pp. 137–147, ISBN 3-8322-5524-9.
- [24] C. Thornton, S. J. Cummins, P. W. Cleary, An investigation of the comparative behaviour of alternative contact force models during elastic collisions, *Powder Technology* 210 (3) (2011) 189–197.
- [25] C. Bierwisch, T. Kraft, H. Riedel, M. Moseler, Three-dimensional discrete element models for the granular statics and dynamics of powders in cavity filling, *Journal of the Mechanics and Physics of Solids* 57 (1) (2009) 10–31.
- [26] H. Hertz, Über die Berührung fester elastischer Körper, *Journal für die reine und angewandte Mathematik* 92 (1881) 156–171.
- [27] E. D. Landau, E. M. Lifshitz, *Theory of Elasticity*, Pergamon Press, 1970.
- [28] J. U. Brackbill, D. B. Kothe, C. Zemach, A continuum method for modeling surface tension, *Journal of Computational Physics* 100 (2) (1992) 335–354.
- [29] T. B. Anderson, R. Jackson, A fluid mechanical description of fluidized beds, *Industrial & Engineering Chemistry Fundamentals* 6 (4) (1967) 527–539.
- [30] M. Mezhericher, A. Levy, I. Borde, Heat and mass transfer of single droplet/wet particle drying, *Chemical Engineering Science* 63 (1) (2008) 12–23.
- [31] J. U. Brackbill, D. B. Kothe, *Dynamical modeling of surface tension*, Tech. rep., Los Alamos National Lab., NM (United States) (1996).
- [32] B. Lafuire, C. Nardone, R. Scardovelli, S. Zaleski, G. Zanetti, Modelling merging and fragmentation in multiphase flows with surfer, *Journal of Computational Physics* 113 (1994) 134–147.
- [33] D. J. E. Harvie, M. R. Davidson, M. Rudman, An analysis of parasitic current generation in volume of fluid simulations, *Australian and New Zealand Industrial and Applied Mathematics Journal* 46 (E) (2005) C133–C149.
- [34] P. K. Kundu, I. M. Cohen, *Fluid mechanics*, Academic Press (Elsevier), 2008, ISBN 978-0-12-373735-9.
- [35] M. Fujita, O. Koike, Y. Yamaguchi, Direct simulation of drying colloidal suspension on substrate using immersed

- free surface model, *Journal of Computational Physics* 281 (2015) 421 – 448.
- [36] G. Bertrand, C. Filiatre, H. Mahdjoub, A. Foissy, C. Coddet, Influence of slurry characteristics on the morphology of spray-dried alumina powders, *Journal of the European Ceramic Society* 23 (2) (2003) 263 – 271.
- [37] T. Breinlinger, A. Hashibon, T. Kraft, Simulation of the spray drying of single granules: The correlation between microscopic forces and granule morphology, *Journal of the American Ceramic Society*(accepted for publication).
- [38] H. Mahdjoub, P. Roy, C. Filiatre, G. Bertrand, C. Coddet, The effect of the slurry formulation upon the morphology of spray-dried yttria stabilised zirconia particles, *Journal of the European Ceramic Society* 23 (10) (2003) 1637 – 1648.